Research Square

Preprints are preliminary reports that have not undergone peer review.
They should not be considered conclusive, used to inform clinical practice,
or referenced by the media as validated information.

Silica Aerogel as an Active Residue Modifier in Intumescent Coatings: Balancing Thermal Insulation, Adhesion and Char Evolution

Yujia Fan
University College London
Nima Roeinfard
Brunel University of London
Yanzhuo Li
University College London
Ziwei Chen
University College London
Kewei Chen
University College London
Georgios Nikiforidis
University College London
Adham Hashibon
University College London
Buddha Deka Boruah
University College London
Kostas Grigoriadis
University College London
Mingqing Wang
mingqing.wang@ucl.ac.uk

University College London

Article

Keywords: Silica aerogel, Intumescent coating, Thermal barrier, Pull-off adhesion

Posted Date: September 3rd, 2026

DOI: https://doi.org/10.21203/rs.3.rs-10787655/v1

License: This work is licensed under a Creative Commons Attribution 4.0 International License.
Read Full License

Additional Declarations: No competing interests reported.

Abstract

Silica aerogels offer exceptional thermal insulation, but their integration into intumescent fire-protective coatings presents a fundamental trade-off between thermal performance, mechanical integrity, and high-temperature char stability. Here, we incorporate a commercial hydrophobic silica aerogel at 0–20 wt% into two waterborne intumescent formulations (BS and SM) and systematically evaluate their thermal, mechanical, and high-temperature performance. At 15 wt% loading, thermal conductivity reaches 0.088 W m^{-1} K^{-1} (BS) and 0.091 W m^{-1} K^{-1} (SM)—representing reductions of 84.7% and 77.4% versus neat coatings—while transient heat transfer to the underlying metal substrate is delayed by up to 9.6°C. However, pull-off adhesion retention falls to 46–48% at 15wt% and further deteriorates to 15–18% at 20 wt%, revealing a critical thermal–mechanical trade-off. Notably, aerogel acts not as an inert filler but as an active modifier of high-temperature residue evolution, exhibiting strongly matrix-dependent behaviour: it suppresses expansion in BS, producing compact sintered residues (~ 9% contraction at 800°C), whereas SM retains open fibrous architectures. Finite-element simulations corroborate the application of the optimised coating for practical thermal bridging protection, identifying a conductivity criterion ($k < 0.035$ W m^{-1} K^{-1}) required to achieve net thermal benefit in mineral-wool-insulated assemblies. We conclude that 15wt% aerogel loading provides the optimal balance between insulation, adhesion and high-temperature integrity. These findings establish silica aerogel as an active residue modifier rather than a passive filler, providing a rational formulation strategy for next-generation intumescent coatings that simultaneously address fire protection and building energy performance.

Introduction

Intumescent coatings constitute a primary passive protection strategy for metallic structures subjected to rapid temperature rise during fire exposure (Zhan et al. 2024; Fu et al. 2025). Although steel has a high melting point, it loses structural strength at 400–500°C, so thermal management is needed to prevent collapse. Fire safety regulations accordingly mandate passive protection to maintain load-bearing capacity for 60–120 minutes, enabling safe evacuation and firefighting. Char thermal conductivity is the decisive property here: lower values reduce heat flux to the steel, extending time to critical failure. Thus, minimising coating conductivity, while preserving mechanical integrity enhances life safety, asset protection and infrastructure resilience. Upon heating, these coatings undergo a cascade of dehydration, decomposition, gas release and subsequent char formation, producing an expanded porous layer that restricts heat transfer to the underlying substrate. The protective efficacy of such coatings depends not only on the volumetric expansion ratio, but equally on the thermal conductivity, structural cohesion, pore architecture and substrate adhesion of the resulting char layer (Bond et al. 2026). While highly expanded residues can offer substantial thermal resistance, excessive foaming frequently yields fragile, discontinuous or poorly adhered chars that are prone to cracking and interfacial detachment (Xiao et al. 2025). This inherent trade-off between thermal insulation and mechanical integrity remains a central challenge in developing high-performance intumescent systems.

Silica aerogels have emerged as highly compelling thermal-insulation additives because of their exceptionally low density, high porosity and ultra-low thermal conductivity (Randall et al. 2011; Cuce et al. 2014). Their nanoscale porous architecture effectively suppresses both solid-phase and gas-phase heat conduction, making them ideal candidates for lightweight insulation materials and thermally functional coatings. Nevertheless, the incorporation of silica aerogel into waterborne intumescent formulations is fraught with difficulties. Hydrophobic aerogel particles often exhibit limited compatibility with aqueous binder systems, while their high specific volume substantially dilutes the effective binder fraction. During fire exposure, binder dilution degrades melt rheology; low viscosity favours gas escape over controlled expansion, producing thinner, less tortuous char with poorer insulation. At elevated loadings, particle agglomeration, non-uniform dispersion, excessive porosity and weak aerogel-matrix interfaces collectively degrade dry-state coating adhesion and structural coherence (Li et al. 2025a). Under fire-induced thermal gradients, micro-defects become macroscopic failure sites: poor adhesion promotes char delamination, while aerogel agglomerates concentrate stress and initiate through-thickness cracking. Such chars are vulnerable to hose impact, structural vibrations and thermal cycling any of which can spall the layer and expose bare steel. In the specific context of intumescent coatings, silica aerogel can additionally modify melt viscosity, gas retention behaviour, char expansion dynamics and inorganic-phase redistribution during thermal assault. Consequently, the relationship between aerogel loading and thermal protection is inherently non-linear, with increasing additive content not securing a monotonic improvement, and with failure modes transitioning from a gradual loss of insulation efficiency at moderate loadings to catastrophic protective-layer detachment at excessive loadings.

Previous studies have examined silica aerogel as a low-conductivity filler in polymeric or fire-retardant coatings, predominantly within a single coating matrix or narrow concentration windows (Di et al. 2022; Li et al. 2025b). Far less attention has been given to the coupled effect of aerogel loading on thermal transport, adhesion and high-temperature residue evolution across different distinct commercial intumescent formulations. This comparative perspective is critical because aerogel behaviour depends on the host coating's binder chemistry, intumescent package, inorganic fillers and reinforcing fibres. Determining whether a universal optimum loading exists, and how the aerogel modifies different char-forming matrices, is necessary for rational formulation design.

In this work, a commercial hydrophobic silica aerogel was incorporated at ~ 20 wt% into two waterborne intumescent coating matrices, denoted BS and SM. The modified coatings were characterised using X-ray diffraction (XRD), Fourier-transform infrared spectroscopy (FTIR), scanning electron microscopy coupled with energy-dispersive X-ray spectroscopy (SEM-EDX), thermogravimetric analysis (TGA), thermophysical measurements, infrared thermography and pull-off adhesion test. The relationship between aerogel concentration, thermal conductivity, transient heat-transfer and coating adhesion was investigated. Microstructural and elemental evolution before and after furnace exposure at 800°C in air was further examined to elucidate char formation in the two matrices. The results reveal a non-monotonic thermal response, a pronounced thermal-mechanical trade-off, and strongly matrix-

dependent residue evolution, providing practical guidance for selecting aerogel loadings that enhance thermal-barrier performance without unduly compromising coating integrity.

Results & Discussion

2.1 Preparation and characterization of silica aerogel-modified intumescent coatings

The preparation route and proposed thermal-barrier mechanism is illustrated in Fig. 1a. Quartzene® Z1H1 silica aerogel (denoted as SA), was incorporated into two commercial intumescent coating matrices, Brosteel Ultra 60 (BS) and SteelMaster 600WF (SM). Owing to its low bulk density and hydrophobic surface, SA was first dispersed in 2-propanol by ultrasonication before mixing into the as-received BS or SM coating. The formulations were mechanically blended until visually homogeneous, applied onto cleaned metal substrates, and dried under identical conditions. A series of BS- and SM-based coatings with nominal SA loadings of 0, 5, 10, 15 and 20 wt% were prepared. As shown in Fig. 1b, the low-density porous SA increased the thermal resistance of the coating by introducing additional air-filled regions and disrupting continuous solid-phase heat-transfer pathways, thereby delaying heat transfer to the underlying metal substrate. Increasing the SA loading also reduced the effective binder fraction and introduced additional aerogel-matrix interfaces, which could compromise coating cohesion and adhesion. The formulation design therefore seeked an optimum SA concentration that balances thermal insulation against structural integrity.

Figure 2 presents the morphological, structural and thermal characteristics of the silica aerogel powder and the two intumescent coating systems. As shown in Figs. 2a **– c**, SA consisted of irregular micron-sized agglomerates assembled from finer silica particles, producing a rough and hierarchically porous surface. This aggregated morphology is consistent with the low bulk density of the aerogel powder and provides numerous internal and interparticle pores that may suppress heat-transfer after incorporation into the coating matrices. Cross-sectional SEM images of the neat coatings revealed distinct matrix-dependent morphologies. BS exhibited a heterogeneous cellular structure with rounded and irregular macropores, alongside with a relatively dense surface layer (Figs. 2d **– f**). At higher magnification, plate-like crystalline particles and finer fibrous or particulate components were observed within the matrix. The neat SM coating showed a similarly cellular morphology, although its pore walls were rougher and displayed a more pronounced fibrous and plate-like inorganic network (Figs. 2g **– i**). This baseline microstructure and filler distribution may underlie the distinct density, thermal transport and adhesion behaviour of the two commercial coating matrices.

The XRD patterns (Fig. 2j**)** show that SA exhibited a broad diffraction halo centred at ~ 22°, confirming its predominantly amorphous structure (Huang et al. 2018). In contrast, neat BS and SM displayed multiple sharp reflections, indicating crystalline intumescent additives and inorganic pigments. Reflections in the low-angle region were assigned to overlapping contributions from ammonium polyphosphate (PDF#82–0918), pentaerythritol (PDF#03-0214) and melamine (PDF#24-1654). Peaks from rutile TiO_2 (PDF#76-

1940) appeared in both coatings, while additional reflections from hexagonal ZnO (PDF#89-1397) were identified in BS (Hasannezhad et al. 2024). After incorporating 15 wt% SA, the principal diffraction positions remained largely unchanged, though the amorphous background in the 20 ~ 25° region intensified. No new crystalline phases were detected, confirming that SA was incorporated as an amorphous dispersed phase without inducing detectable bulk crystalline reactions.

The FTIR spectra in Fig. 2k further corroborate SA incorporation. The SA spectrum was dominated by a broad and intense absorption band at approximately 1050 ~ 1100 cm^{-1}, assigned to asymmetric amorphous Si–O–Si stretching. Weaker features near 1250 and 800 cm^{-1} correspond to surface Si–CH_3 groups and symmetric Si–O–Si vibrations, respectively, consistent with the hydrophobic methylated surface of SA (Yi et al. 2019). Neat BS and SM coatings exhibited an ester carbonyl band near 1730 cm^{-1} from the polymeric binder, alongside CH_2/CH_3 deformation bands and possible ammonium-group vibrations in the 1450 ~ 1380 cm^{-1} region. The broad absorption region between 1250 and 1000 cm^{-1} contains overlapping contributions from P–O, P–O–P and C–O vibrations associated with intumescent additives and binder (Baena et al. 2023). Following 15 wt% SA addition, the 1100 ~ 1000 cm^{-1} region became broader and more intense because of the additional Si–O–Si contribution, while the main bands of the original coating matrices remained present and no new absorption bands were observed. This indicates that SA was incorporated mainly through physical dispersion and interactions rather than formation of a new bulk chemical structure.

The thermal-decomposition behaviour under nitrogen (Fig. 2l) shows that SA exhibited notably high thermal stability, retaining approximately 75% of its initial mass at 800°C. Its limited mass loss arises from removal of adsorbed species and decomposition of surface methyl groups, while the silica framework remained as the predominant inorganic residue. In contrast, the BS- and SM-based coatings underwent multistage degradation. The initial low-temperature mass loss was associated with residual moisture and volatile species, followed by the principal decomposition region at approximately 250 ~ 450°C, during which the polymeric binder and intumescent components decomposed, released gas and formed condensed-phase char. Above this region, the samples exhibited gradual mass loss from further char evolution and residual organic degradation.

SA incorporation increased the residual mass of both coating systems at 800°C, reflecting the contribution of the thermally stable silica phase. The SA-containing formulations exhibited changes in the principal degradation region, indicating that the aerogel modified the overall thermal-decomposition behaviour. However, the increased residue should not be interpreted solely as enhanced char formation, as part of the increase results directly from the higher inorganic fraction introduced by SA. A mass-weighted mixture-rule between experimental and predicted residues is therefore required before claiming synergistic char-stabilisation.

Overall, the combined SEM, XRD and FTIR results confirm that SA acts as a porous, amorphous silica phase while the principal crystalline and chemical features of the matrices were retained. The TGA results further show that SA increased the high-temperature solid fraction of both coating systems.

These structural and thermal changes underpin the reduced density and heat-transfer rate of the SA-modified coatings, although their practical benefit must be weighed against the reduction in pull-off strength at high SA loadings.

2.2 Mechanical and thermophysical properties

Figure 3 summarises the pull-off adhesion and thermophysical properties of the BS- and SM-based coatings as a function of SA loading. Pull-off adhesion tests were performed using a laboratory-scale method adapted from ASTM D4541-22(2022a). A loading fixture bonded to the coating surface was subjected to a progressively increasing tensile load normal to the substrate until failure (Fig. 3a**)**. The pull-off strength was calculated from the maximum force and bonded area. As shown in Fig. 3b, neat SM coating exhibited higher pull-off strength than neat BS, with values of 2.249 and 1.727 MPa, respectively. Incorporation of 15 wt% SA reduced the strength to 1.040 MPa for SM and 0.823 MPa for BS, retaining approximately 46.2% and 47.7% of their original values. Further increasing SA to 20 wt% caused pronounced deterioration to 0.408 MPa for SM and 0.270 MPa for BS, retaining only 18.1% and 15.6% of the neat-coating strengths. This reduction is attributed to the decreasing effective binder fraction, increased porosity and weak aerogel-matrix interfaces at elevated SA loadings. The consistently higher strength of the SM-based system suggests better matrix cohesion or interfacial compatibility with the metal substrate.

The density of the coatings decreased progressively with increasing SA content, as shown in Fig. 3c. BS density dropped from 1.24 to 0.54 g cm^{-3}, while SM decreased from approximately 1.16 to 0.54 g cm^{-3} at 20 wt% SA. A reduction of over 50%, consistent with the extremely low bulk density of the aerogel. In contrast, the mass-specific heat capacity changed only moderately with SA loading (Fig. 3d). The estimated C_p of BS decreased slightly from 0.781 to 0.771 J g^{-1} K^{-1}, whereas that of SM decreased from 1.334 to 1.213 J g^{-1} K^{-1}. This gradual variation indicates that thermal conductivity changes were governed primarily by reductions in density and thermal diffusivity, rather than by large C_p shifts.

As shown in Fig. 3e, the thermal diffusivity decreased substantially with SA incorporation, reaching a minimum at 15 wt% for both matrices. The diffusivity of BS decreased from 0.594 to 0.200 mm^2 s^{-1}, while that of SM decreased from 0.260 to 0.109 mm^2 s^{-1}. At 20 wt%, diffusivities increased to 0.284 and 0.148 mm^2 s^{-1} for BS and SM, respectively. A corresponding non-monotonic trend was observed in the calculated thermal conductivity (Fig. 3f). The minimum values of 0.088 W m^{-1} K^{-1} for BS-15SA and 0.091 W m^{-1} K^{-1} for SM-15SA represent reductions of approximately 84.7% and 77.4%, respectively, relative to the neat coatings. At 20 wt%, conductivity rose to 0.118 W m^{-1} K^{-1} and 0.097 W m^{-1} K^{-1}, respectively.

The deterioration above 15 wt% may arise from aerogel agglomeration, non-uniform binder distribution, structural defects or additional solid-contact pathways within the dried coatings. Together with the severe adhesion loss at 20 wt%, these results indicate that excessive SA loading compromises both

homogeneity and mechanical integrity. Among the investigated formulations, 15 wt% SA provides the most favourable balance between thermal insulation and retained adhesion, although the decrease in strength relative to the neat coatings remains substantial.

Figure 4 presents the infrared thermograms and centre-point temperature responses of stainless-steel substrates protected by BS- and SM-based coatings containing 0, 15, and 20wt% SA. Sample temperature rose rapidly during the initial stage of hot-plate exposure, then increased more gradually as the coating-substrate assemblies approached thermal equilibrium. SA-containing coatings consistently exhibited lower centre temperatures than their neat counterparts, confirming that the porous aerogel phase delayed heat transfer to the underlying metal.

Within the BS-based series, BS-15SA exhibited the lowest temperature throughout the entire heating period. Its centre temperature increased from 29.5°C at 5 s to 55.5°C at 30 s and 63.4°C at 120 s, compared with 37.2, 65.1 and 71.1°C for BS-0SA, corresponding to temperature reductions of 7.7, 9.6 and 7.7°C. Although BS-20SA also outperformed the neat coating, its temperatures remained consistently higher than those of BS-15SA, indicating that increasing the SA content beyond 15 wt% did not yield further improvement and instead diminished the thermal-protection efficiency of the BS-based coating.

A similar, though less pronounced, effect was observed in the SM-based system. Both SM-15SA and SM-20SA exhibited lower temperatures than SM-0SA. At 120 s, the centre temperatures of SM-15SA and SM-20SA were 65.4 and 65.6°C, respectively, compared with 70.0°C for the neat SM coating. The small difference between the 15 and 20 wt% coatings suggests that the thermal-barrier benefit approached a plateau above 15 wt% SA in the SM matrix. Given experimental variability arising from difference in coating thickness, surface roughness and thermal contact, the two SA-containing SM formulations should therefore be regarded as having broadly comparable transient thermal responses.

The infrared thermography results are consistent with the calculated thermal-conductivity data, particularly for the BS-based coatings, where both the minimum thermal conductivity and the lowest backside temperature occurred at 15 wt% SA. The superior performance at this loading likely stems from the combined reduction in coating density and thermal diffusivity, together with disruption of continuous solid-phase heat-transfer pathways. At 20wt% SA, aerogel agglomeration, non-uniform binder distribution and structural defects may partially offset the benefits of the additional porous phase. Together with the substantial loss in adhesion observed at 20wt%, these factors identify 15wt% SA as the more favourable thermal–mechanical compromise within the investigated formulation range.

2.3 High-temperature evolution of the coating microstructures

Figure 5 compares the cross-sectional and high-magnification morphologies of the BS- and SM-based coatings before and after furnace exposure. Coated stainless steel discs were heated in air from room

temperature to 800°C at 10°C min^{-1}, held for 20 min and cooled before morphological examination. Prior to heating, neat BS exhibited a relatively uniform porous structure with numerous rounded voids and a fine network of short needle-like components. In contrast, neat SM contained coarser and longer fibrous or rod-like constituents alongside plate-like particles. These larger reinforcing features may contribute to mechanical bridging and partially account for the higher pull-off strength of the neat SM coating.

Upon furnace exposure, neat BS and SM coatings underwent extensive intumescence, forming highly expanded, lightweight and snowflake-like residues. However, the resulting char layers were extremely fragile and largely detached from the metal substrates. The post-heating SEM images capture only a small fraction of the original expanded residue. At higher magnification, the retained char consisted of thin flakes, open voids and fractured cellular walls, indicating that high expansion was accompanied by poor mechanical integrity. Consequently, the residual thickness after testing cannot be used to determine the maximum expansion achieved by the neat coatings.

Silica aerogel incorporation markedly altered the high-temperature behaviour of the BS-based coatings. Unlike neat BS, BS-15SA and BS-20SA did not develop highly expanded and fluffy residues. Instead, the remaining layers appeared more contracted and compact, with granular, rounded and interconnected inorganic-rich domains visible at higher magnification. This morphology is consistent with a sintering-like thermal consolidation process, in which the silica-rich phase restricted foam growth and promoted denser residue formation. The effect was particularly evident for BS-20SA. Based on the 200× cross-sectional SEM images, in which the image height approximately spans the coating thickness, the local thickness decreased from approximately 1.06 mm before heating to 0.96 mm after heating, corresponding to an apparent thickness retention of approximately 91% (i.e., a contraction of about 9%). Considering the rough interfaces and uncertainty associated with boundary selection, the estimated contraction is more appropriately expressed as approximately 5 ~ 15%.

A different response was observed for the SM-based coatings. Both SM-15SA and SM-20SA retained open cellular and fibrous char structures after heating, indicating that the intumescent process was not fully suppressed by SA. The expanded residues contained interconnected membranes, elongated ligaments and relatively large pores. SM-20SA exhibited somewhat thicker and more folded cell walls, suggesting greater consolidation at the higher SA loading. The persistence of the open char network may be related to the coarser and longer fibrous constituents initially present in SM, which could provide structural support during expansion and subsequent shrinkage.

Overall, the results demonstrate a pronounced matrix-dependent effect of SA on char development. In the BS system, SA inhibited expansion and produced a compact, thermally consolidated residue, whereas in the SM system it was incorporated into a still-expanded fibrous char framework. Although the SA-containing coatings retained more coherent residues than the neat formulations, interfacial gaps and local debonding remained visible, consistent with the substantial adhesion loss at elevated SA loadings. These observations emphasise that maximum intumescence alone does not guarantee effective

protection; an appropriate balance among char expansion, structural cohesion and substrate adhesion is required.

Figure 6 presents SEM images, corresponding EDX maps of C, O, Si and P, and map-sum spectra (summarized in Table 1) of the SA-containing BS- and SM-based coatings before and after furnace exposure. Prior to heating, all four elements were distributed throughout the coating matrices, consistent with the incorporation of the silica-rich SA phase into the phosphate-containing intumescent formulations. Nevertheless, variations in local signal intensity indicate that SA was present as dispersed particles or agglomerates rather than as a completely homogeneous phase.

In the BS-based coatings, furnace exposure produced a pronounced redistribution of the inorganic constituents. BS-15SA retained O-, Si- and P-containing regions throughout the consolidated residue, although the maps showed greater local concentrated after heating. Greater heterogeneity was observed for BS-20SA, where the Si- and P-containing phases appeared highly localised within the analysed region. This elemental heterogeneity is consistent with the contracted and sintering-like residue observed by SEM and suggests localised inorganic consolidation and possible phase segregation at high SA loading(Table 1). The reduced mapping intensity in individual regions should not be interpreted as evidence of bulk elemental loss, as the post-heating residue was highly heterogeneous and only a local field of view was analysed.

In contrast, the SM-based coatings retained a more interconnected elemental distribution following furnace treatment. In SM-15SA and SM-20SA, C, O, Si and P were distributed along the cellular walls and fibrous ligaments of the expanded residue. The persistence of Si and O throughout the open char framework indicates that the silica-rich phase became remained incorporated within the expanded structure without completely suppressing intumescence. The spatial association of Si- and P-containing regions suggests that the silica and phosphate phases may have jointly contributed to the inorganic framework, though EDX mapping alone cannot establish the formation of specific Si–O–P chemical bonds.

Overall, the EDX results indicate a matrix-dependent high-temperature redistribution of SA. The BS system developed a comparatively heterogeneous and consolidated inorganic residue, whereas the SM system retained a more continuous Si- and P-containing cellular framework. These observations support the different char morphologies identified by SEM and provide further insight into the contrasting high-temperature responses of the two commercial matrices.

The map-sum compositions are interpreted as semi-quantitative measurements because they represent local analysed regions and may be influenced by elemental normalisation, sample mounting and the limited accuracy of EDX for light elements.

Table 1
Summary of elemental compositions (wt%) obtained from EDX map-sum spectra.

Element (wt%)	C	O	Si	P
BS-15SA Before	56.1	33.0	10.4	0.50
BS-15SA After	39.6	32.0	17.4	11.0
BS-20SA Before	52.8	34.5	12.7	0.00
BS-20SA After	53.6	40.1	5.00	1.30
SM-15SA Before	45.4	38.6	12.2	3.80
SM-15SA After	47.2	41.8	8.00	3.00
SM-20SA Before	50.8	31.0	18.2	0.00
SM-20SA After	39.8	36.2	12.7	11.2

To evaluate the practical applicability of the silica-aerogel-modified intumescent coating in building applications, two-dimensional steady-state finite-element thermal simulations were performed for two representative steel connection designs using a coating with thermal conductivity of approximately 0.09 W m^{-1} K^{-1}. The Geometrical Configurations, Boundary Conditions, and Material Assignments for the two designs can be found in **Figure S1** and the material properties assigned to the numerical models are summarized in **Table S1** .The coating thickness was parametrically varied from 0 to 20 mm, and the thermal response was evaluated in terms of heat-transfer rate (Q), minimum internal surface temperature ($T_{s\ min}$), two-dimensional thermal coupling coefficient (L_{2D}), internal surface temperature factor (f_{RSI}), and linear thermal transmittance (Ψ).

As shown in Table 2, for Design 21684, Ψ increased by 95.5% (0.061 to 0.119 W·m⁻¹·K⁻¹) and Q increased by 14.7% (9.876 to 11.331 W), while T□,□,□ decreased from 19.41 to 19.08°C, thereby increasing the potential for surface condensation. This behaviour arises because the formulated coating (k = 0.09 W/m·K) is more conductive than the mineral wool insulation (k = 0.035 W/m·K) that it covers; as the coating thickness increase, a greater thickness of low-conductivity insulation is replaced by the higher-conductivity nanocomposite coating, thereby increasing heat flow. The same trend was observed for Design 21683 (Ψ: +33.2%, Q: +20.2%), with the larger deterioration in Design 21684 reflecting the greater influence of the localised conduction path on heat transfer. Supplementary Figures S2 and S3 further illustrate the temperature distributions and heat flux contours for Designs 21684 and 21683, respectively, confirming that the coating primarily mitigates localized heat flux concentration around the steel connection rather than substantially modifying the overall wall temperature field. These results indicate a conductivity criterion for achieving a net thermal benefit under the simulated material-replacement condition: increasing coating thickness can provide a thermal benefit only when $k_{coating} < k_{mineral\ wool}$. For mineral wool (≈ 0.035 W/m·K), the 15 wt% SA coating (≈ 0.09 W/m·K) is approximately 2.5 times more

conductive than the insulation, explaining the increase in heat transfer. Although this formulation represents a significant 77–85% reduction in thermal conductivity relative to the neat coatings, it remains insufficient to provide a net thermal benefit in mineral-wool-insulated assemblies. A coating conductivity below approximately 0.035 $W \cdot m^{-1} \cdot K^{-1}$ would therefore be required under the present material-replacement scenario.

However, still lower thermal conductivity through increased SA loading is constrained by adhesion: increasing SA loading beyond 15wt% reduces pull-off strength to 15–18% of the neat value at 20wt%. Thus, higher aerogel loadings may reduce the coating conductivity towards the required threshold, but potentially at the expense of mechanical integrity. Practically, designers should therefore apply such coatings at the minimum thickness required for fire protection, while addressing thermal bridging through geometry optimisation, thermal breaks, or additional insulation. Increasing coating thickness beyond the fire-protection requirement should be avoided where the coating is more conductive than the insulation it replaces, as this may adversely affect the thermal performance of the building envelope.

Table 2
Effect of Coating Thickness on the Thermal Performance of Designs 21684 and 21683

Design	Coating Thickness (mm)	Heat Transfer, Q (W)	Minimum Surface Temperature, $T_{s,min}$ (°C)	2D Thermal Coefficient, L_{2D} ($W \cdot m^{-1} \cdot K^{-1}$)	Internal Surface Temperature Factor, f_{RSI}	Linear Thermal Transmittance, Ψ ($W \cdot m^{-1} \cdot K^{-1}$)
21684	0.00	9.8758	19.412	0.39503	0.93648	0.06095
	0.20	9.8564	19.401	0.39426	0.93604	0.06018
	1.00	9.9002	19.392	0.39601	0.93568	0.06193
	5.00	10.137	19.338	0.40548	0.93352	0.07140
	10.0	10.466	19.265	0.41864	0.93060	0.08456
	15.0	10.850	19.184	0.43400	0.92736	0.09992
	20.0	11.331	19.084	0.45324	0.92336	0.11916
21683	0.00	7.8861	19.177	0.31544	0.92708	0.19177
	0.20	7.9228	19.177	0.31691	0.92708	0.19324
	1.00	7.9699	19.162	0.31879	0.92648	0.19513
	5.00	8.2336	19.073	0.32934	0.92292	0.20568
	10.0	8.6046	18.951	0.34418	0.91804	0.22051
	15.0	9.0208	18.811	0.36083	0.91244	0.23716
	20.0	9.4757	18.629	0.37903	0.90516	0.25536

Conclusion

This study systematically demonstrates that silica aerogel incorporation into waterborne intumescent coatings delivers substantial reductions in thermal conductivity, with a maximum reduction of 84.7% at 15wt% SA loading, while simultaneously imposing significant penalties on mechanical adhesion, with only 46–48% of the original pull-off strength retained. Crucially, we reveal that aerogel acts not as an inert low-conductivity filler but as an active modifier of high-temperature residue evolution, exerting strongly matrix-dependent effects: suppression of expansion and formation of compact sintering-like residues in BS, compared with preservation of open, fibrous char architectures in SM. Finite-element simulations further evaluated the application of the optimised coating in practical thermal-bridging scenarios. The simulations identified a conductivity criterion for achieving a net thermal benefit: increased coating thickness is beneficial only when the coating thermal conductivity remains below that of the insulation it replaces (≈ 0.035 W m^{-1} K^{-1} for mineral wool). The 15wt% aerogel formulation (≈ 0.09 W m^{-1} K^{-1}), while representing a 77–85% reduction in thermal conductivity relative to the neat coatings, remains insufficient to provide a net thermal benefit in standard mineral-wool-insulated assemblies, indicating that further reductions in thermal conductivity and/or alternative application strategies are required to optimise building energy performance.

We conclude that 15 wt% silica aerogel loading represents the most favourable thermal–mechanical compromise within the investigated range, providing the greatest thermal-conductivity reduction while retaining comparatively higher mechanical integrity than the 20 wt% formulation. Our findings establish that effective functional additive design in intumescent systems requires simultaneous consideration of thermal transport, binder rheology, char mechanics, and matrix-specific residue evolution. The integrated experimental–simulation framework developed here provides a rational pathway for designing next-generation intumescent coatings that simultaneously address the critical dual demands of fire protection and building energy efficiency, with potential relevance to sustainable infrastructure and building-sector carbon reduction.

Declarations

Author Contribution

Y.F. performed the experimental investigation, formal analysis, and wrote the original draft. N.R. led the thermal modelling and simulation work and co-wrote the original draft. Y.L., Z.C., and K.C. contributed to the experimental investigation, especially surface area and porosity analysis, and reviewed the manuscript. G.N. and B.D.B. contributed to review the manuscript. A.H. contributed to the thermal modelling discussion and manuscript review. K.G. and M.W. conceived the study, secured funding, supervised the project, and led the final manuscript revision and polishing. All authors reviewed and approved the final manuscript.

Acknowledgement

The authors would like the funding support from the EPSRC Impact Acceleration Account (IAA) award “Minimising Thermal Bridging with Epoxy Silica Xerogel Coated Façade Components.”This project was undertaken in collaboration with industry project partners Interface Facade Engineering (IFE) Ltd (Will Stevens, Tasos Poulokefalos, and Oliver Grady).

References

1. Baena JC, Wang C, Kabir II, et al (2023) Fire behaviour of waterborne intumescent coatings on timber substrate for bushfire exposure. Fire Saf J 140:103836. https://doi.org/10.1016/j.firesaf.2023.103836
2. Bond E, Murphy A, Millen SLJ (2026) Investigating the heating rate response of a hybrid intumescent coating up to 1000°C: A multi-technique experimental analysis. Mater Today Commun 52:114998. https://doi.org/10.1016/j.mtcomm.2026.114998
3. Cuce E, Cuce PM, Wood CJ, Riffat SB (2014) Toward aerogel based thermal superinsulation in buildings: A comprehensive review. Renewable and Sustainable Energy Reviews 34:273–299. https://doi.org/10.1016/j.rser.2014.03.017
4. Di Z, Ma S, Wang H, et al (2022) Modulation of Thermal Insulation and Mechanical Property of Silica Aerogel Thermal Insulation Coatings. Coatings 12:1421. https://doi.org/10.3390/coatings12101421
5. Fu A, Ulusoy B, Ahmadi H, et al (2025) Intumescent coatings: Comprehensive advances with a focus on inorganic-dominant systems. Prog Org Coat 199:108939. https://doi.org/10.1016/j.porgcoat.2024.108939
6. Hasannezhad A, Amirpoor S, Dolati A, Sharifi R (2024) Boosting the efficiency of water-based intumescent coatings with fumed silica nanoparticles: A synergistic approach. Mater Today Commun 41:111126. https://doi.org/10.1016/j.mtcomm.2024.111126
7. Huang D, Zhang M, Shi L, et al (2018) Effects of particle size of silica aerogel on its nano-porous structure and thermal behaviors under both ambient and high temperatures. Journal of Nanoparticle Research 20:308. https://doi.org/10.1007/s11051-018-4419-8
8. Li C, Xu H, Guo C, et al (2025a) Thermal performance mechanisms of n-octadecane composite phase change materials (PCM) enhanced by hydrophilic and hydrophobic silica-based aerogels. Journal of Building Engineering 115:114533. https://doi.org/10.1016/j.jobe.2025.114533
9. Li Z, Chen Z, Duan Y, et al (2025b) A review of silica aerogel based thermal insulation coatings: Preparation, properties and applications. Prog Org Coat 208:109449. https://doi.org/10.1016/j.porgcoat.2025.109449
10. Randall JP, Meador MAB, Jana SC (2011) Tailoring Mechanical Properties of Aerogels for Aerospace Applications. ACS Appl Mater Interfaces 3:613–626. https://doi.org/10.1021/am200007n
11. Xiao F, He W, Shao W, et al (2025) Natural tannic acid-based intumescent coating towards efficient fire resistance and thermal performance for steel structure. Int J Biol Macromol 322:146983.

https://doi.org/10.1016/j.ijbiomac.2025.146983
12. Yi Z, Tang Q, Jiang T, Cheng Y (2019) Adsorption performance of hydrophobic/hydrophilic silica aerogel for low concentration organic pollutant in aqueous solution. Nanotechnol Rev 8:266–274. https://doi.org/10.1515/ntrev-2019-0025
13. Zhan W, Li L, Chen L, et al (2024) Biomaterials in intumescent fire-retardant coatings: A review. Prog Org Coat 192:108483. https://doi.org/10.1016/j.porgcoat.2024.108483
14. (2022a) Test Method for Pull-Off Strength of Coatings Using Portable Adhesion Testers
15. (2022b) Test Method for Thermal Diffusivity by the Flash Method

Figures

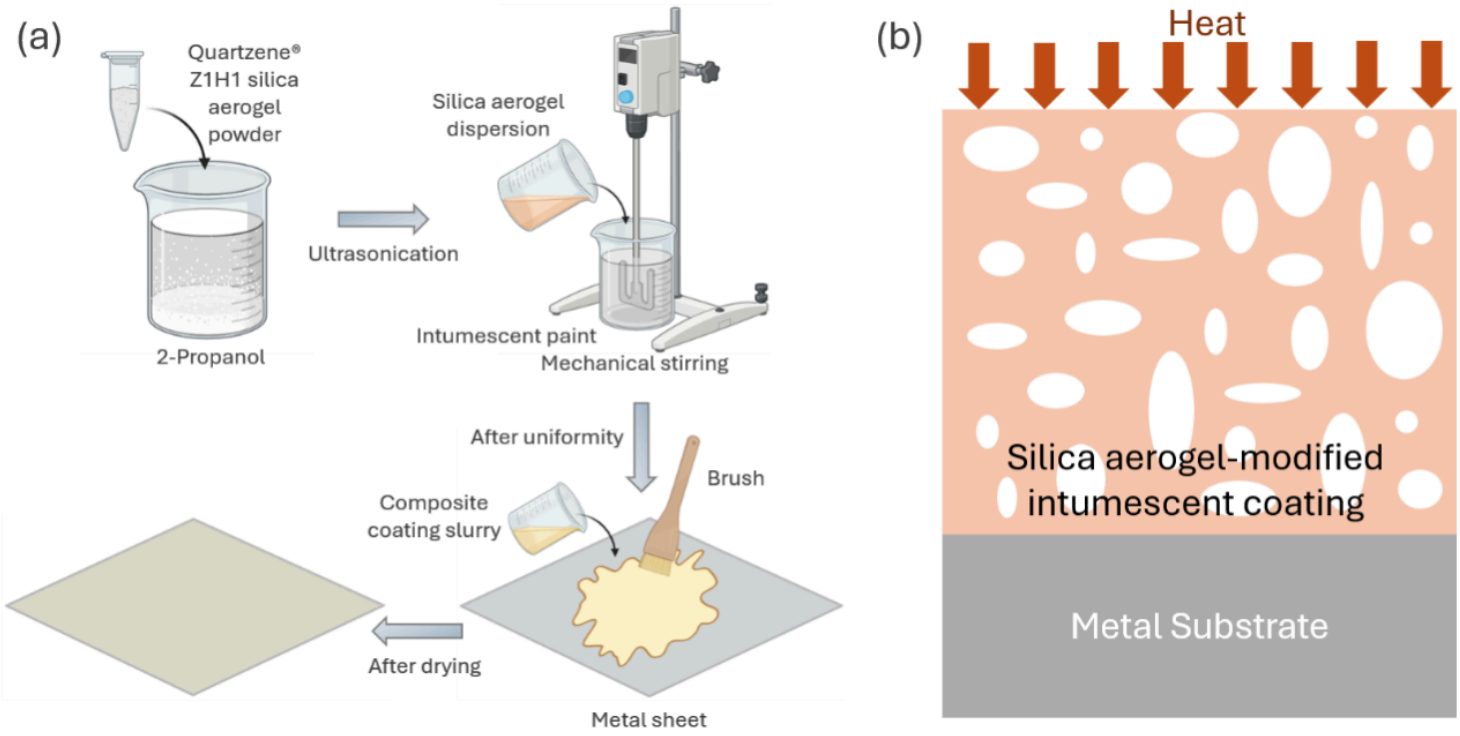


Figure 1

Schematic illustration of silica aerogel-modified intumescent coating fabrication and proposed thermal-barrier mechanism. (a) Preparation and application of the aerogel-containing coating. (b) Porous coating structure for reducing heat transfer to the metal substrate.

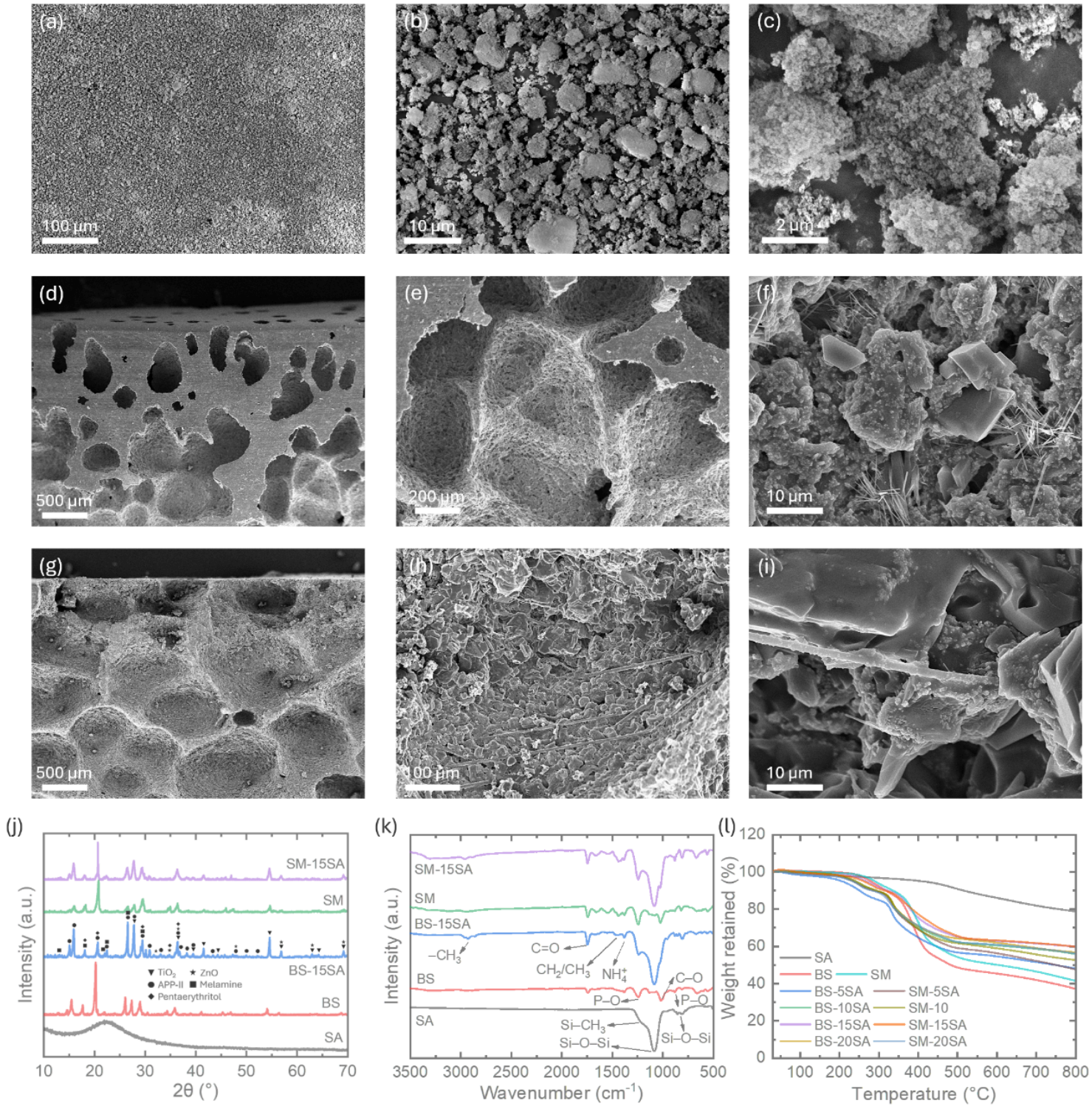


Figure 2

Morphological, structural and thermal characterisation of silica aerogel powder and intumescent coating systems. Cross-sectional SEM images of (a–c) silica aerogel powder, (d–f) neat BS, and (g–i) SM intumescent coatings. (j) XRD patterns and (k) FTIR spectra of SA, BS, BS-15SA, SM and SM-15SA. (l) TGA curves of intumescent coatings with varying SA content.

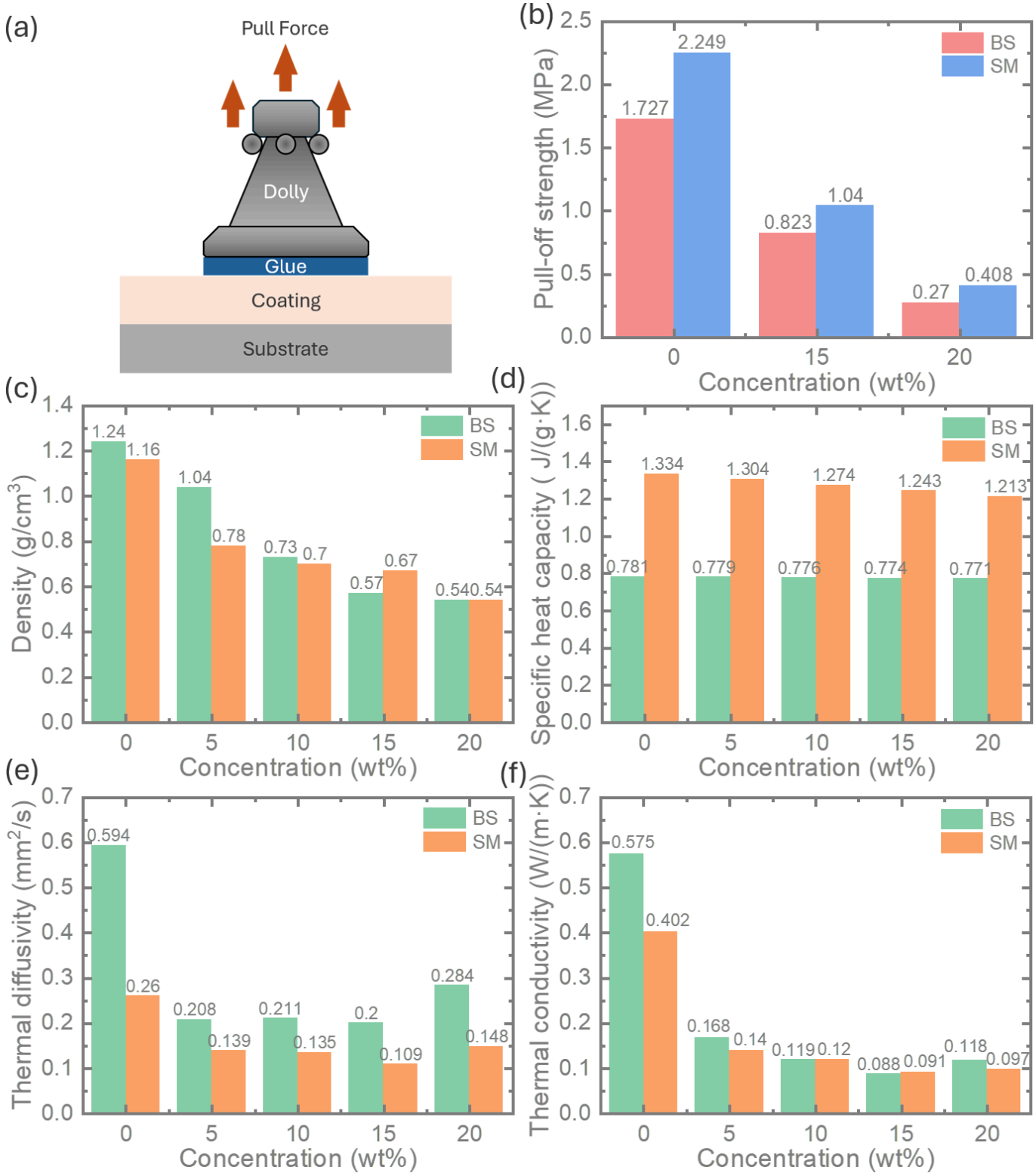


Figure 3

Mechanical and thermophysical properties of silica aerogel-modified BS- and SM-based intumescent coatings. (a) Schematic of the pull-off adhesion test. (b) Pull-off strength of the neat, 15 wt% SA and 20 wt% SA formulations. (c) Density, (d) estimated specific heat capacity, (e) Thermal diffusivity and (f) Thermal conductivity as functions of SA loading. The specific heat capacities of the composite coatings were

estimated using a mass-weighted mixture rule, and the thermal conductivities were calculated according to $k=\rho\alpha C_p$*(2022b).*

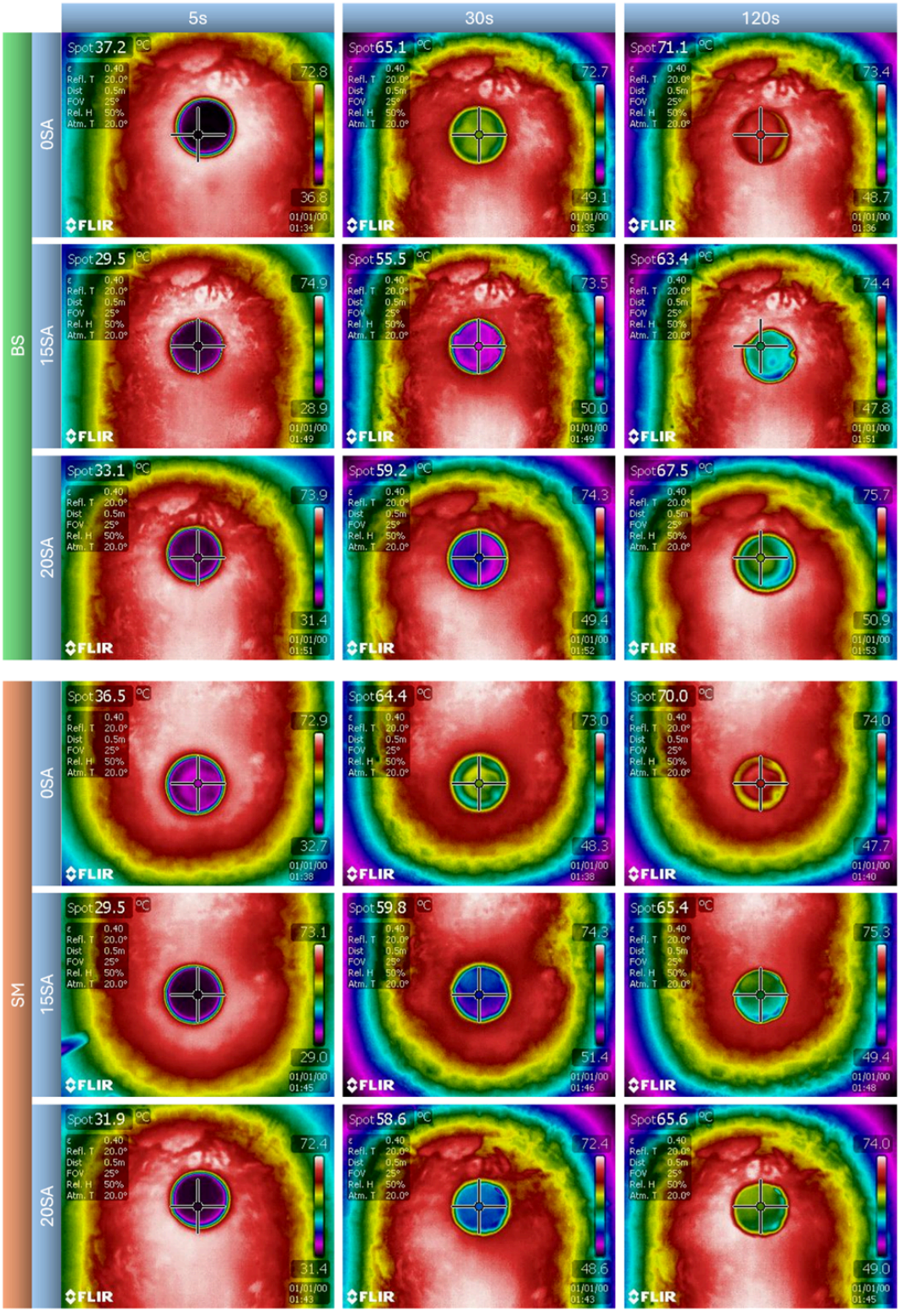


Figure 4

Infrared thermograms of metal substrates protected by BS- and SM-based intumescent coatings containing 0, 15 and 20 wt% silica aerogels after 5, 30 and 120 s of hot-plate exposure. The centre spot temperature of

each coating-substrate assembly is indicated in the corresponding image.

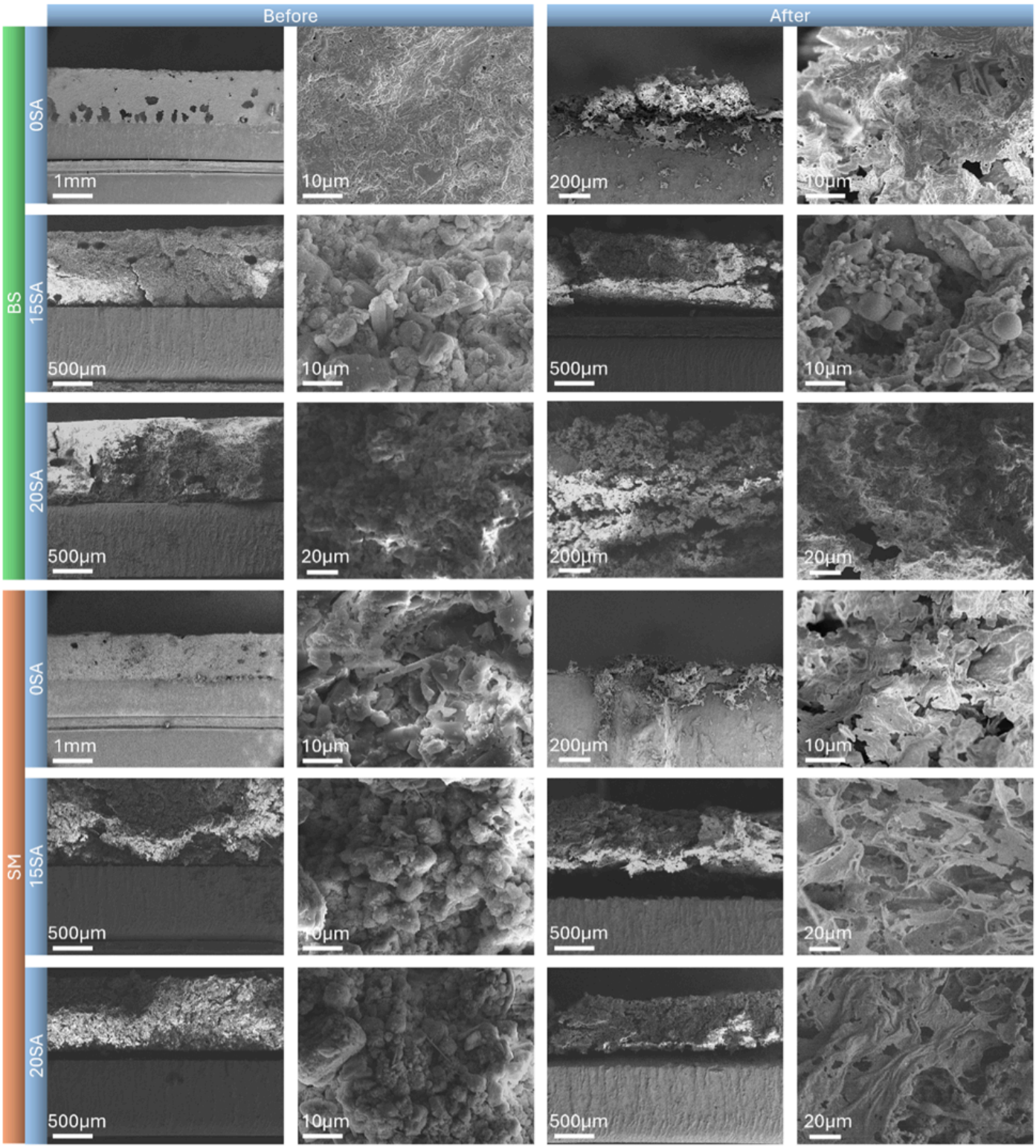


Figure 5

Cross-sectional and high-magnification SEM images of BS- and SM-based intumescent coatings containing 0, 15 and 20 wt% SA before and after furnace exposure (heated in air to 800 °C at 10 °C min⁻¹, held for 20 min).

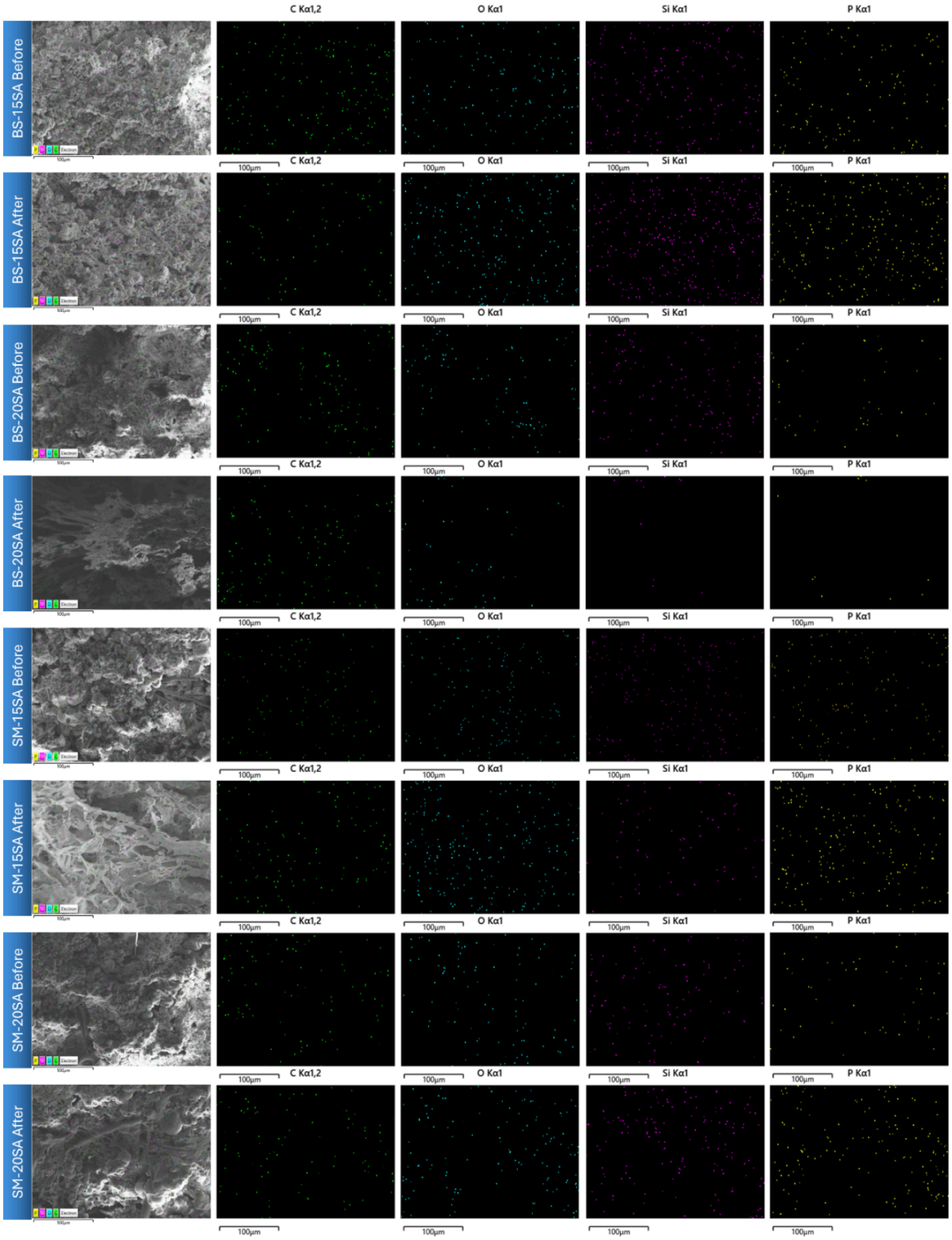


Figure 6

SEM images, corresponding EDX elemental maps of C, O, Si and P for BS-15SA, BS-20SA, SM-15SA and SM-20SA before and after furnace exposure(scalebar=100um).

Supplementary Files

This is a list of supplementary files associated with this preprint. Click to download.

- SupportInformation260816.docx